



# Mid-infrared surface plasmon resonance sensor based on photonic crystal fibers

CHAO LIU,<sup>1,\*</sup> LIN YANG,<sup>1</sup> XILI LU,<sup>2</sup> QIANG LIU,<sup>1</sup> FAMEI WANG,<sup>2</sup> JINGWEI LV,<sup>1</sup> TAO SUN,<sup>3</sup> HAIWEI MU,<sup>1</sup> AND PAUL K. CHU<sup>4</sup>

<sup>1</sup>School of Electronics Science, Northeast Petroleum University, Daqing 163318, China

<sup>2</sup>School of Materials Science and Chemical Engineering, Harbin Engineering, Harbin 150001, China

<sup>3</sup>Institute of Microelectronics, Agency of Science, Technology and Research (A\*STAR), 117685, Singapore

<sup>4</sup>Department of Physics and Materials Science, City University of Hong Kong, Tat Chee Avenue, Kowloon, Hong Kong, China

\*msm-liu@126.com

**Abstract:** A surface plasmon resonance (SPR) sensor with two open-ring channels based on a photonic crystal fiber (PCF) is described. The sensor is designed to detect low refractive indexes between 1.23 and 1.29 with the operation wavelength in mid-infrared region between 2550 nm and 2900 nm. The coupling characteristics and sensing properties are numerically analyzed by the finite element method. The average spectral sensitivity is 5500 nm/RIU and a maximum resolution of  $7.69 \times 10^{-6}$  RIU can be obtained. Our analysis shows that the PCF-SPR sensor is suitable for mid-infrared detection.

© 2017 Optical Society of America

**OCIS codes:** (060.2280) Fiber design and fabrication; (240.6680) Surface plasmons; (060.5295) Photonic crystal fibers.

## References and links

1. A. G. Brolo, "Plasmonics for future biosensors," *Nat. Photonics* **6**(11), 709–713 (2012).
2. A. A. Rifat, G. A. Mahdiraji, Y. M. Sua, R. Ahmed, Y. G. Shee, and F. R. M. Adikan, "Highly sensitive multi-core flat fiber surface plasmon resonance refractive index sensor," *Opt. Express* **24**(3), 2485–2495 (2016).
3. L. G. Carrascosa, A. A. I. Sina, R. Palanisamy, B. Sepulveda, M. A. Otte, S. Rauf, M. J. A. Shiddiky, and M. Trau, "Molecular inversion probe-based SPR biosensing for specific, label-free and real-time detection of regional DNA methylation," *Chem. Commun. (Camb.)* **50**(27), 3585–3588 (2014).
4. X. Li, Y. Wang, J. Luo, and S. Ai, "Sensitive detection of adenosine triphosphate by exonuclease III-assisted cyclic amplification coupled with surface plasmon resonance enhanced fluorescence based on nanopore," *Sens. Actuators B Chem.* **228**, 509–514 (2016).
5. C. Lertvachirapaiboon, A. Baba, S. Ekgasit, K. Shinbo, K. Kato, and F. Kaneko, "Transmission surface plasmon resonance imaging of silver nanoprisms enhanced propagating surface plasmon resonance on a metallic grating structure," *Sens. Actuators B Chem.* **249**, 39–43 (2017).
6. G. Di Noto, A. Bugatti, A. Zandrini, E. L. Mazzoldi, A. Montanelli, L. Caimi, M. Rusnati, D. Ricotta, and P. Bergese, "Merging colloidal nanoplasmonics and surface plasmon resonance spectroscopy for enhanced profiling of multiple myeloma-derived exosomes," *Biosens. Bioelectron.* **77**, 518–524 (2016).
7. E. Kretschmann and H. Raether, "Radiative decay of non-radiative surface plasmons excited by light," *Z. Naturforsch. A* **23**(12), 2135–2136 (1968).
8. J. N. Dash and R. Jha, "Graphene based birefringent photonic crystal fiber sensor using surface plasmon resonance," *IEEE Photonics Technol. Lett.* **26**(11), 1092–1095 (2014).
9. C. Caucheteur, T. Guo, and J. Albert, "Review of plasmonic fiber optic biochemical sensors: improving the limit of detection," *Anal. Bioanal. Chem.* **407**(14), 3883–3897 (2015).
10. J. Hsu, S. Jeng, and Y. Sun, "Simulation and experiments for optimizing the sensitivity of curved D-type optical fiber sensor with a wide dynamic range," *Opt. Commun.* **341**, 210–217 (2015).
11. Y. Shevchenko, C. Chen, M. A. Dakka, and J. Albert, "Polarization-selective grating excitation of plasmons in cylindrical optical fibers," *Opt. Lett.* **35**(5), 637–639 (2010).
12. A. Hassani and M. Skorobogatiy, "Photonic crystal fiber-based plasmonic sensors for the detection of bio-layer thickness," *J. Opt. Soc. Am. B* **26**(8), 1550–1557 (2009).
13. M. Hautakorpi, M. Mattinen, and H. Ludvigsen, "Surface-plasmon-resonance sensor based on three-hole microstructured optical fiber," *Opt. Express* **16**(12), 8427–8432 (2008).
14. X. Xin, S. Li, T. Cheng, W. Qin, and J. Xue, "Numerical simulation of surface plasmon resonance based on Au-metalized nanowires in the liquid-core photonic crystal fibers," *Optik (Stuttg.)* **126**(15-16), 1457–1461 (2015).

15. D. Gao, C. Guan, Y. Wen, X. Zhong, and L. Yuan, "Multi-hole fiber based surface plasmon resonance sensor operated at near-infrared wavelengths," *Opt. Commun.* **313**(4), 94–98 (2013).
16. G. Wang, S. Li, G. An, X. Wang, Y. Zhao, W. Zhang, and H. Chen, "Highly sensitive D-shaped photonic crystal fiber biological sensors based on surface plasmon resonance," *Opt. Quantum Electron.* **48**(1), 46 (2016).
17. G. An, S. Li, X. Yan, X. Zhang, Z. Yuan, H. Wang, Y. Zhang, X. Hao, Y. Shao, and Z. Han, "Extra-broad photonic crystal fiber refractive index sensor based on surface plasmon resonance," *Plasmonics* **12**(2), 465–471 (2017).
18. P. B. Johnson and R. W. Christy, "Optical constants of the noble metals," *Phys. Rev. B* **6**(12), 4370–4379 (1972).
19. G. Ghosh, M. Endo, and T. Iwasaki, "Temperature-dependent Sellmeier coefficients and chromatic dispersions for some, optical fiber glasses," *J. Lightwave Technol.* **12**(8), 1338–1342 (1994).
20. A. Hassani and M. Skorobogatiy, "Design criteria for microstructured optical fiber based surface Plasmon resonance sensors," *J. Opt. Soc. Am. B* **24**(6), 1423–1429 (2007).
21. J. Xue, S. Li, Y. Xiao, W. Qin, X. Xin, and X. Zhu, "Polarization filter characters of the gold-coated and the liquid filled photonic crystal fiber based on surface plasmon resonance," *Opt. Express* **21**(11), 13733–13740 (2013).
22. J. Homola, S. S. Yee, and G. Gauglitz, "Surface plasmon resonance sensors: review," *Sens. Actuators B Chem.* **54**(1-2), 3–15 (1999).
23. R. Otupiri, E. K. Akowuah, S. Haxha, H. Ademgil, F. AbdelMalek, and A. Aggoun, "A Novel Birefringent Photonic Crystal Fiber Surface Plasmon Resonance Biosensor," *IEEE Photonics J.* **6**(4), 6801711 (2014).
24. X. Yu, Y. Zhang, S. S. Pan, P. Shum, M. Yan, Y. Leviatan, and C. M. Li, "A selectively coated photonic crystal fiber based surface plasmon resonance sensor," *J. Opt.* **12**, 74–77 (2009).

## 1. Introduction

In surface plasmon resonance (SPR), electromagnetic waves are coupled with free electron oscillations at the interface between a metallic and dielectric medium under p-polarized light radiation [1]. SPR is highly sensitive to variations in the refractive indexes or optical absorption and particularly useful to biosensing due to the label-free and real-time detection of the kinetics of biological processes [2, 3]. Several SPR-based techniques such as SPR-enhanced fluorescence, SPR imaging, and SPR spectroscopy have been developed [4–6] and there has been significant technical progress pertaining to the light modulation methods, sensing elements, and configurations. The conventional SPR sensing structure is based on Kretschmann and Reather's attenuated total reflection (ATR) [7]. However, this structural configuration is bulky because many optical and mechanical components are required and so remote sensing is difficult. Device miniaturization based on the optical fiber platform can overcome the drawbacks of traditional prism-based SPR sensors and it offers many advantages such as simple and flexible optical design, remote sensing capability, continuous analysis, and in situ monitoring [8, 9].

Several types of optical fiber based SPR sensors with different structures including the D-shape [10], TFBG-based [11] and photonic crystal fiber [12] based SPR sensors have been demonstrated experimentally and theoretically. In particular, photonic crystal fibers (PCF) are especially attractive to SPR sensing. During excitation, the light wave exciting a surface plasmon wave changes phases and the phase matching condition between the plasmonic mode and core guided mode for PCF-SPR sensors can be easily satisfied by introducing air holes into the fiber core, thus allowing tuning of the modal refractive index and matching with that of a plasmon. In 2008, Hautakorp et al. proposed a three-hole microstructured optical fiber based SPR sensor with the operation wavelength in the visible regime [13]. The refractive-index resolution of the sensor for aqueous analytes reached  $1 \times 10^4$  which was better than that of optical fiber based SPR sensors. Xin et al. described a gold-filled liquid-core photonic crystal fiber with a spectral sensitivity of 4125 nm/RIU [14] and Guan et al. presented an optical fiber based SPR sensor with gold and TiO<sub>2</sub> bi-layered films as the plasmonic materials [15]. The refractive-index resolution was estimated to be as high as  $2.7 \times 10^5$  RIU and the resonance wavelength was extended to the near-infrared region. Wang et al. reported a sensitive D-shaped PCF-SPR biological sensor with the resonance wavelength ranging between 745 nm and 1470 nm and the refractive index detection was 1.345-1.41 [16]. An et al. investigated an extra-broad PCF refractive index sensor with a triangular

lattice and four large-size channels based on SPR [17]. The detection range of the refractive index was 1.30-1.79 and the resonance wavelength could be increased from 1680 nm to 1870 nm. In most of these studies, PCF-SPR was exploited only in the visible and near-infrared spectral region due to the wide availability of optical materials and efficient light sources and detectors. On the other hand, PCF-SPR sensors with operation wavelengths in the mid-infrared range have seldom been rarely reported.

Herein, a novel PCF-SPR sensor with two open-ring channels is designed and described. A thin gold film is deposited on the wall of the open-rings by physical or chemical methods and the analyte can penetrate the channels through the entrances automatically. The entrance size of the open-rings can be specifically designed according to the molecular size of the analyte serving the function of filtering. The key performance of the sensor is investigated by the finite element method (FEM) based on the COMSOL Multiphysics software. The detection range of refractive indexes is set to be 1.23-1.29 and an average spectral sensitivity of 5500 nm/RIU is demonstrated and a maximum sensing resolution of  $7.69 \times 10^{-6}$  RIU is obtained. Furthermore, the resonance wavelength of the sensor can be extended to the mid-infrared regime between 2,550 nm and 2,900 nm.

## 2. Numerical modeling

Figure 1 displays the cross-section of the sensor consisting of 12 air holes which restrict the energy from transmitting in the fiber core. The radii of air holes in the first-layer and second-layer are  $r_a = 1 \mu\text{m}$  and  $r_b = 0.8 \mu\text{m}$ , respectively. The refractive index of air is fixed at  $n_{air} = 1$  and the radius of the cladding is  $r_c = 8 \mu\text{m}$ . The radius of the analyte channels is  $r_a = 1 \mu\text{m}$  and there are two micro-openings in the left and right analyte channels. Hence, the micro-liquid can flow into the channel and filter analytes larger than the opening. The pitch for the first air layer ring is kept at  $5.5 \mu\text{m}$ . The symbol  $\Lambda$  represents the distance between the inner layer holes and the thickness of gold layer is denoted by  $t_g$ . The refractive index of the analyte ( $n_s$ ) varies between 1.23 and 1.29. A gold layer is selected as the sensitive material in this model and the dielectric function of gold is determined by Drude model [18]. The dielectric constant of gold is described as:

$$\varepsilon(\omega) = \varepsilon_1 + i\varepsilon_2 = \varepsilon_\infty - \frac{\omega_p^2}{\omega(\omega + i\omega_c)} \quad (1)$$

where  $\varepsilon_\infty = 9.75$  is the dielectric constant of gold at high frequency,  $\omega_p = 1.36 \times 10^{16}$  is the plasma frequency of gold, and  $\omega_c = 1.45 \times 10^{14}$  is the scattering frequency of electron [18]. The thickness of the gold layer is tunable from 42 nm to 50 nm. Pure silica is the background materials in the sensor and the refractive index of silica glass is given by the Sellmeier dispersion relation [19]:

$$n^2 - 1 = \frac{0.6961663\lambda^2}{\lambda^2 - (0.0684043)^2} + \frac{0.4079426\lambda^2}{\lambda^2 - (0.1162414)^2} + \frac{0.897479\lambda^2}{\lambda^2 - (9.896161)^2} \quad (2)$$

The finite element method (FEM) based on the COMSOL Multiphysics software is implemented to investigate the mode characteristics. An artificial boundary condition of the perfectly matched layer (PML) is added to the outer computational region to absorb the radiation energy and the confinement loss is defined as follows [20]:

$$\alpha_{loss} = 8.686 \times \frac{2\pi}{\lambda} \text{Im}(n_{eff}) \times 10^4 \text{ (dB/cm)} \quad (3)$$

where  $\lambda$  represents the wavelength of the incident light in vacuum in micrometer ( $\mu\text{m}$ ) and it is proportional to the imaginary part ( $\text{Im}(n_{eff})$ ) of the effective refractive index. The peak indicates the largest energy transmission from the core guided mode to the plasmonic

mode and it can be used to locate the resonance wavelength. In the analysis, we focus on the fundamental mode because a majority of the energy is transmitted in the form of the fundamental mode.

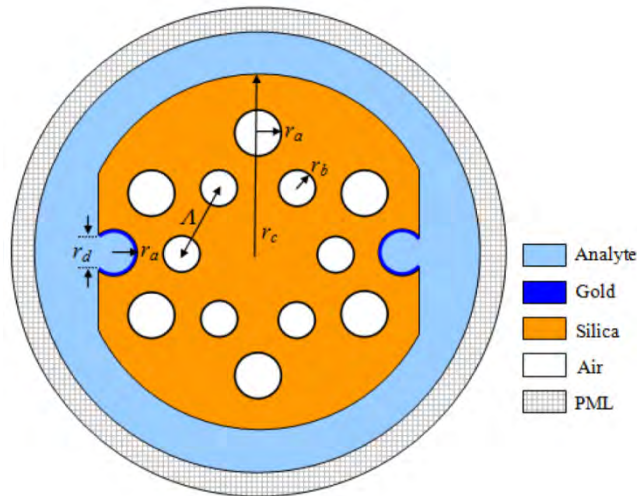
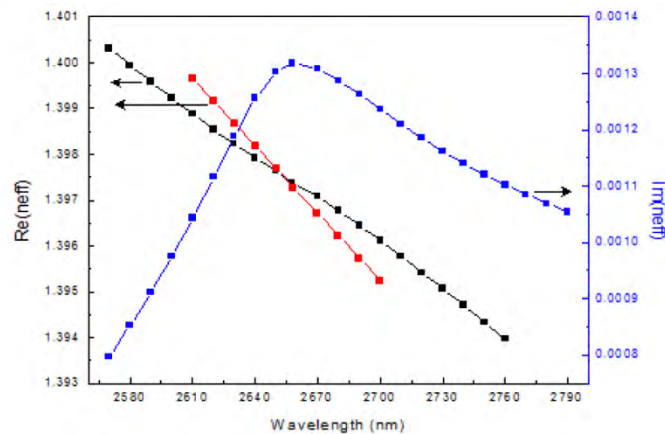


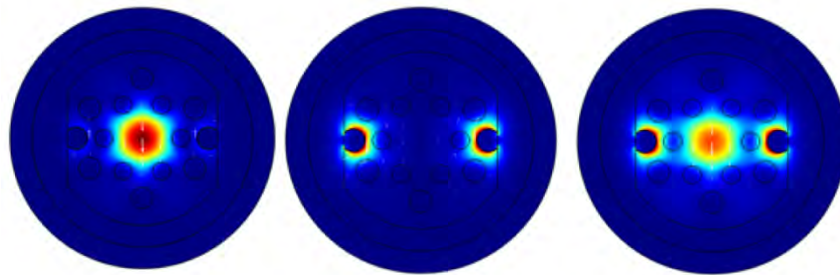
Fig. 1. Cross section of the PCF-SPR sensor.

### 3. Results and discussion

Figure 2(a) shows the distribution of the refractive index of the sensor. The red curve represents the dispersion relation of the plasmonic mode. The black curve which represents the real part of the effective index decreases with increasing wavelength corresponding to the refractive index in the usual sense. The blue curve describes the imaginary part of the refractive index of the fundamental mode. The imaginary part increases initially and then decreases with increasing wavelength. Because the confinement loss is proportional to the imaginary part of the effective refractive index, the variation in the imaginary part directly reflects the mode loss and coupling between the fundamental mode and plasmonic mode. An obvious peak appears at 2658 nm in Fig. 2(a), indicating the occurrence of strong SPR in the mid-infrared wavelength region. The phase matching coupling phenomenon is confirmed by the coincidence of the resonant peak and the intersection between the dispersion relations of the core-guided mode and the plasmonic mode [15]. Figure 2(b) and 2(c) show the optical field distribution of the core-guided mode and plasmonic mode. The optical field of the core-guided mode is distributed entirely in the core, whereas that of the plasmonic mode appears nearly on the surface between the sensing medium and gold film for a given wavelength and refractive index of the analyte. Figure 2(d) presents the optical field distribution of the plasmonic mode and the core-guided mode at resonance wavelength. As shown in Fig. 2(d), largest energy is transferred from the core-guided mode to the plasmonic mode when both modes are strongly coupled.



(a)



(b)

(c)

(d)

Fig. 2. (a) Distribution of the refractive index of the sensor; (b) Optical field distribution (core-guided mode), (c) Optical field distribution (plasmonic mode), (d) optical field distribution (the plasmonic mode and core-guided mode at resonance wavelength), where the arrows indicate the electric field direction. ( $r_a = 1 \mu\text{m}$ ,  $r_b = 0.8 \mu\text{m}$ ,  $r_c = 8 \mu\text{m}$ ,  $t_g = 50 \text{ nm}$ ,  $A = 3.5 \mu\text{m}$ ,  $r_d = 1.2 \mu\text{m}$ , and  $n_s = 1.26$ )

Figure 3 shows the dependence of the loss spectra of the fundamental mode on the thickness of the gold layers. The resonance intensity decreases and the resonance wavelength moves towards shorter wavelengths from 2870 nm to 2660 nm when the thickness of gold layer changes from 42 nm to 50 nm indicative of a blue-shift. A similar phenomenon associated with the blue shift was also noted in literature [21]. In addition, the loss curve shows a sharp resonance peak when the gold layer thickness is 48 nm suggesting that this is the optimal thickness. Based on total internal reflection, the transmitted energy in PCF converges to the central core. The coupling conditions for the plasmonic and core guided modes can be modified by adding air holes. Figure 4 shows the loss spectra of the fundamental mode for different radii of the outer layer air holes between 0.98  $\mu\text{m}$  and 1.02  $\mu\text{m}$ . As shown in Fig. 4, the leaky energy loss exhibits an upward trend initially and then a downward one indicating the occurrence of SPR. The resonance peaks move to a shorter wavelength from 2,720 nm to 2,610 nm.

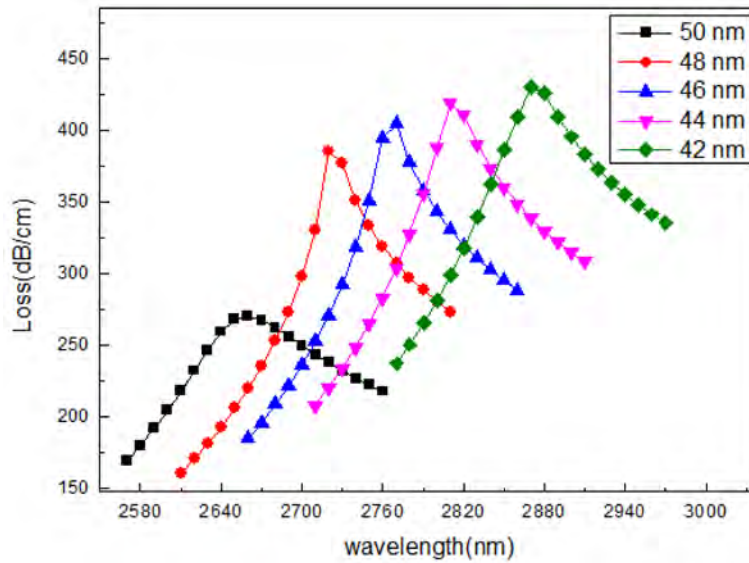


Fig. 3. Dependence of the loss spectra of the fundamental mode on the gold layer thickness ( $r_a = 1 \mu\text{m}$ ,  $r_b = 0.8 \mu\text{m}$ ,  $r_c = 8 \mu\text{m}$ ,  $A = 3.5 \mu\text{m}$ ,  $r_d = 1.2 \mu\text{m}$ , and  $n_s = 1.26$ )

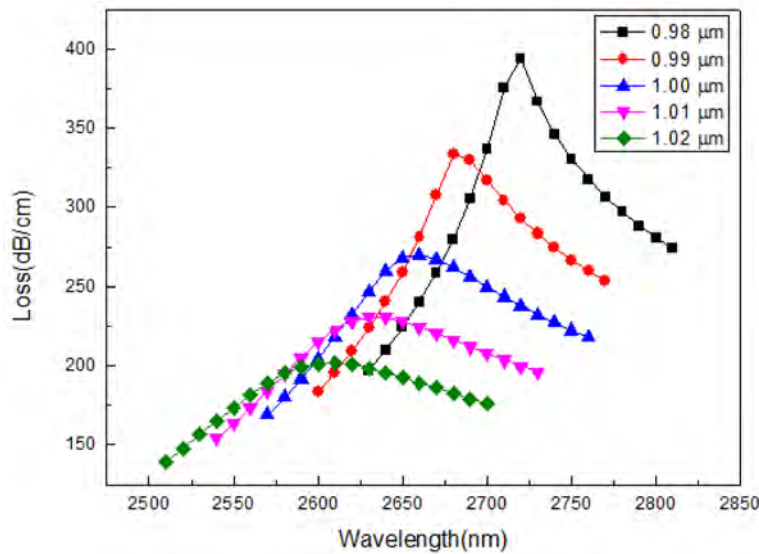


Fig. 4. Loss spectra of the fundamental mode for different radii of the outer layer air holes ( $r_b = 0.8 \mu\text{m}$ ,  $r_c = 8 \mu\text{m}$ ,  $r_d = 1.2 \mu\text{m}$ ,  $A = 3.5 \mu\text{m}$ ,  $t_g = 50 \text{ nm}$ , and  $n_s = 1.26$ )

Figure 5 shows the loss spectra of the fundamental mode for different distances between the inner layer air holes. The distance between the air holes varies from  $3.48 \mu\text{m}$  to  $3.52 \mu\text{m}$ . The resonance wavelengths blue-shift with increasing distance and the half-width of the loss peak increases with distance between air holes as well, revealing that the sensor possesses higher sensitivity at a distance of  $3.48 \mu\text{m}$ .

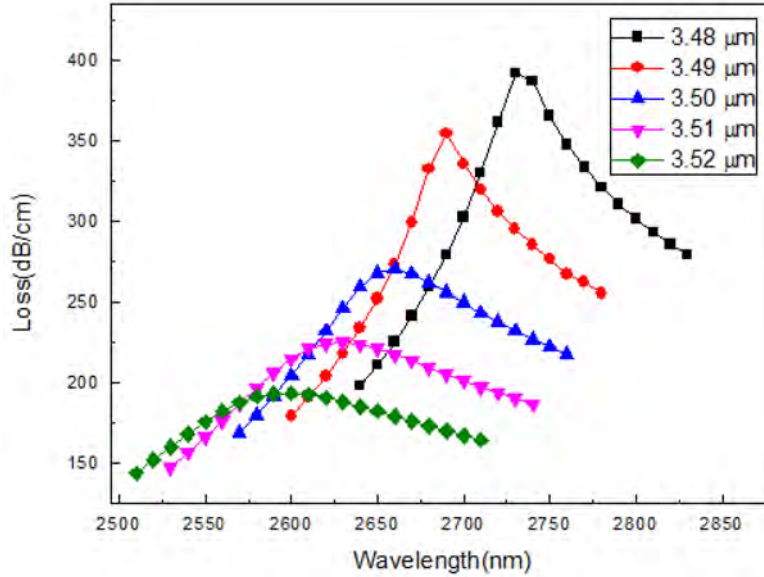


Fig. 5. Loss spectra of the fundamental mode for different distances between inner layer air holes ( $r_a = 1 \mu\text{m}$ ,  $r_b = 0.8 \mu\text{m}$ ,  $r_c = 8 \mu\text{m}$ ,  $r_d = 1.2 \mu\text{m}$ ,  $t_g = 50 \text{ nm}$ , and  $n_s = 1.26$ )

Figure 6 presents the loss spectra of the fundamental mode for different size of the open slots. The resonance intensity increases gradually and the resonance peak becomes sharper when the size of the incision changes from  $1.428 \mu\text{m}$  to  $0.872 \mu\text{m}$ , indicating stronger coupling between the plasmonic and core-guided modes. Furthermore, the resonance wavelength blue-shifts from  $2,730 \text{ nm}$  to  $2,640 \text{ nm}$  when the size of the incisions rises from  $0.872 \mu\text{m}$  to  $1.428 \mu\text{m}$ . Therefore, the performance of the sensor can be optimized by adjusting the size of the incisions. In addition, it is seen from Fig. 2(d) that the local electric field enhancement is mainly concentrated on the inner walls of the analyte channels at resonance wavelength. According to the phase matching conditions, the wave number of the surface plasmon wave is sensitive to the ambient analyte as follows [22]:

$$\text{Re}\{K_{sp}\} = \left\{ \frac{\omega}{c} \sqrt{\frac{\varepsilon_m(\lambda) \cdot n^2}{\varepsilon_m(\lambda) + n^2}} \right\} \quad (4)$$

The refractive index of the analyte can be detected by the resonance wavelength and so the sensor can effectively monitor the refractive index of the analyte liquid flowing into the opening ring channels. Suppose that the analyte liquid contains two kinds of organic molecules. One kind of molecule is smaller than the opening slots and the other is larger than the opening slots. The sensor can function as a filter to selectively detect the concentration of organic molecules such as bacteria that are smaller than the incision of the rings.

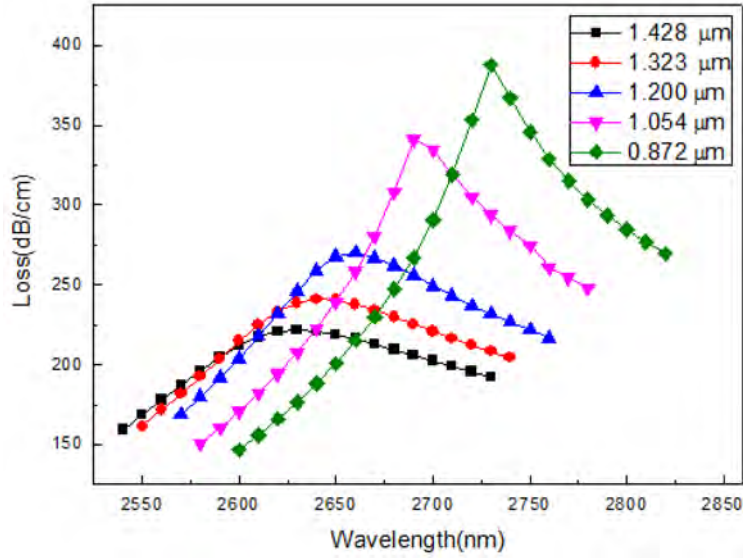


Fig. 6. Loss spectra of the fundamental mode for different size of the open slots ( $r_a = 1 \mu\text{m}$ ,  $r_b = 0.8 \mu\text{m}$ ,  $r_c = 8 \mu\text{m}$ ,  $A = 3.5 \mu\text{m}$ ,  $t_g = 50 \text{ nm}$ , and  $n_s = 1.26$ )

Figure 7 depicts the wavelength dependence of the loss spectra on the refractive index of the analyte. The resonant peak shifts to longer wavelengths and the moving distance also increases gradually when the refractive index increases from 1.23 to 1.29. The resonance wavelengths can be tuned between 2,550 nm and 2,900 nm. Since there is no secondary peak, the sensor is more suitable for sensing. The spectral sensitivity is one of the most important parameters and expressed as [12]:

$$S(\lambda) = \frac{\Delta\lambda_{peak}}{\Delta n_a} (nm/RIU) \quad (5)$$

where  $\Delta\lambda_{peak}$  and  $\Delta n_a$  represent the resonance wavelength changes and refractive index variation, respectively. As shown in Fig. 7,  $\Delta\lambda_{peak}$  is about 55 nm on the average and  $\Delta n_a$  is 0.01 [23, 24]. Therefore, an average spectral sensitivity of 5500 nm/RIU can be achieved for the refractive index range between 1.23 and 1.29. The spectral sensitivity can reach as high as 13,000 nm/RIU for the partial refractive index range between 1.28 and 1.29. The refractive index of resolution is another important parameter of the sensor and is defined as [13]:

$$R = \Delta n_a \Delta\lambda_{min} / \Delta\lambda_{peak} \quad (6)$$

where  $\Delta\lambda_{min}$  represents the wavelength resolution assumed to be 0.1 nm. When the refractive index of the analyte changes to 0.01, a sensing resolution of  $7.69 \times 10^{-6}$  RIU is achieved.

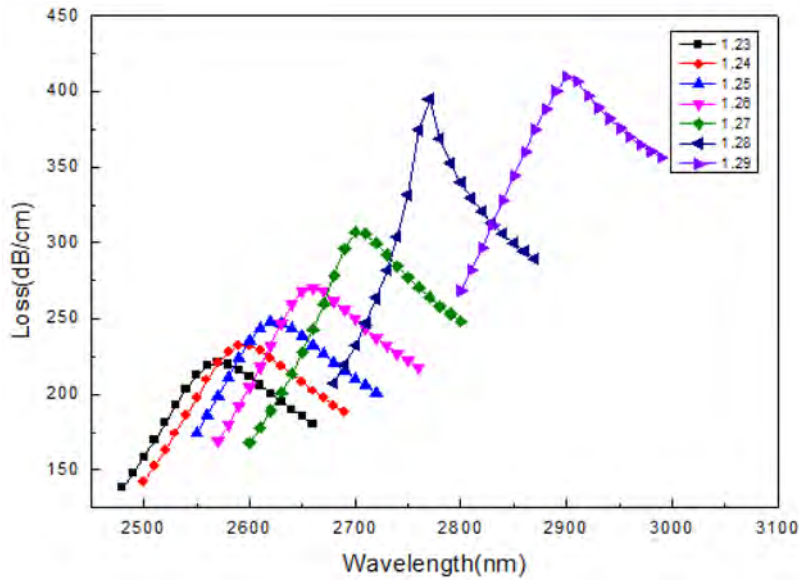


Fig. 7. Loss spectra of the fundamental mode for different refractive indexes of the analyte ( $r_a = 1 \mu\text{m}$ ,  $r_b = 0.8 \mu\text{m}$ ,  $r_c = 8 \mu\text{m}$ ,  $r_d = 1.2 \mu\text{m}$ ,  $t_g = 50 \text{ nm}$ , and  $A = 3.5 \mu\text{m}$ )

Alternatively, amplitude sensitivity  $S(\lambda)$  is another crucial parameter to evaluate the performance of the sensor, where only measurement at single wavelength is needed for analyte detection. Amplitude sensitivity can be defined as [20]:

$$S(\lambda) = \frac{1}{\alpha(\lambda, n_a)} \frac{\partial \alpha(\lambda, n_a)}{\partial n_a} (\text{RIU}^{-1}) \quad (7)$$

where  $\partial \alpha(\lambda, n_a)$  is the difference between two adjacent loss spectrum due to a small change in refractive index of the analyte,  $\alpha(\lambda, n_a)$  is the confinement loss,  $\partial n_a$  is the change of refractive index of the analyte. The amplitude sensitivity curves of the sensor are shown in Fig. 8 for different refractive indexes of the analyte. There is a maximum amplitude sensitivity existing in each curve. The maximum amplitude sensitivity rises from  $132 \text{ RIU}^{-1}$  to  $210 \text{ RIU}^{-1}$  when the refractive index varies from 1.25 to 1.28, indicating that the interaction between evanescent field and the plasmonic mode increases with the increase of refractive index of the analyte. Meanwhile, the resonance wavelength where the maximum value is located red-shifts from 2590 nm to 2700 nm.

Additionally, the amplitude sensitivity depends strongly on the thickness of a gold layer. The dependences of amplitude sensitivity on gold thickness are shown in Fig. 9. For the sensor with a constant gold thickness, the amplitude sensitivity increases firstly and then decreases with the wavelength. The amplitude sensitivity curves move towards shorter wavelength as the gold thickness increases from 42 nm to 50 nm. The maximum amplitude sensitivity corresponding to the gold thickness of 50 nm, 48 nm, 46 nm, 44 nm, and 42 nm is  $206.7 \text{ RIU}^{-1}$ ,  $299.3 \text{ RIU}^{-1}$ ,  $306.5 \text{ RIU}^{-1}$ ,  $318.3 \text{ RIU}^{-1}$ , and  $333.8 \text{ RIU}^{-1}$ , respectively. Because gold thickness becomes larger, the core-guided mode becomes effectively screened from a plasmon, resulting in a low coupling efficiency and low sensitivity [20]. Therefore, it can be concluded that a maximum amplitude sensitivity of  $333.8 \text{ RIU}^{-1}$  can be obtained by tailoring the gold thickness at 42 nm.

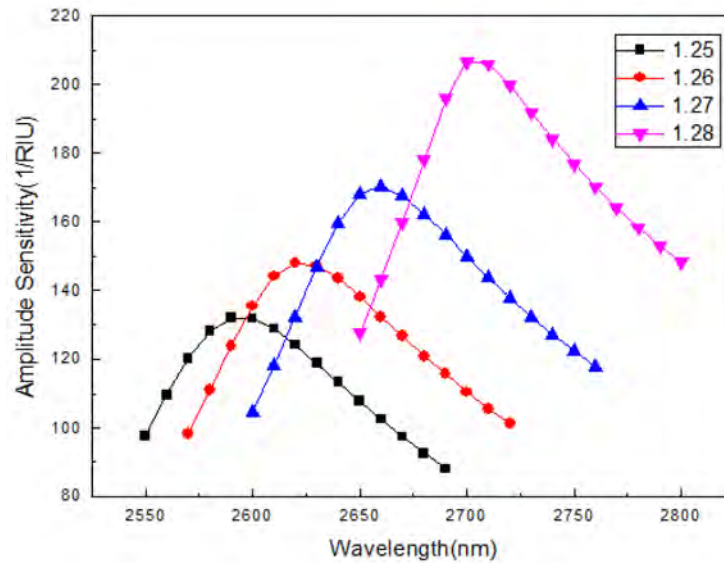


Fig. 8. Amplitude sensitivity of the sensor for different refractive indexes of the analyte ( $r_a = 1 \mu\text{m}$ ,  $r_b = 0.8 \mu\text{m}$ ,  $r_c = 8 \mu\text{m}$ ,  $r_d = 1.2 \mu\text{m}$ ,  $t_g = 50 \text{ nm}$ , and  $\Lambda = 3.5 \mu\text{m}$ )

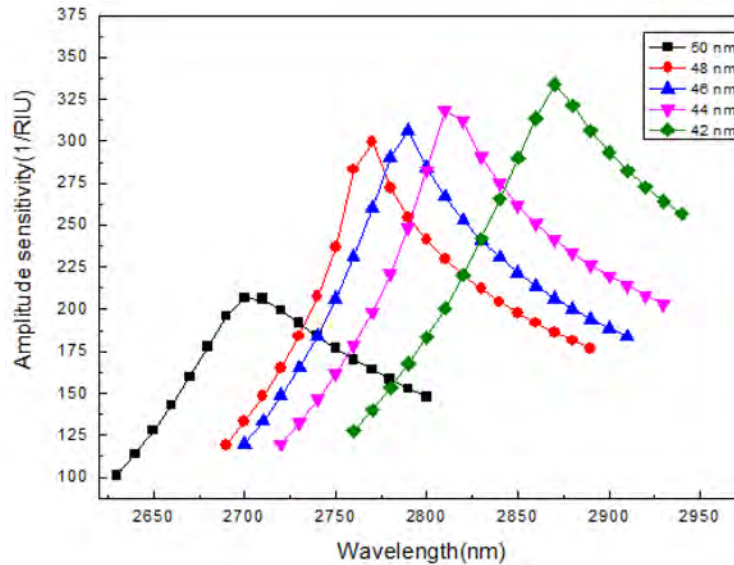


Fig. 9. The dependences of amplitude sensitivity of the sensor on gold thickness ( $r_a = 1 \mu\text{m}$ ,  $r_b = 0.8 \mu\text{m}$ ,  $r_c = 8 \mu\text{m}$ ,  $r_d = 1.2 \mu\text{m}$ ,  $n_s = 1.26$ , and  $\Lambda = 3.5 \mu\text{m}$ )

#### 4. Conclusions

A novel PCF-SPR sensor is designed and analyzed. The analyte channel in the sensor consists of two openings rings thereby making it easier to metallize by depositing plasmonic materials onto the inner wall of the open rings. The analyte flows into the liquid channel automatically when the sensor is inserted into the container thus eliminating the need for infusing a liquid into the analyte channel. Our theoretical assessment reveals that the spectral sensitivity and amplitude sensitivity of the sensor can reach  $5500 \text{ nm/RIU}$  and  $333.8 \text{ RIU}^{-1}$ , respectively. A sensing resolution of  $7.69 \times 10^{-6} \text{ RIU}$  is obtained. In this way, the resonance wavelengths can be extended to the mid-infrared region between  $2,550 \text{ nm}$  and  $2,900 \text{ nm}$  and

the unique opening ring channels serve as a molecule filter for selective detection of organic molecules with different concentrations.

### **Funding**

Natural National Science Foundation of China (NSFC) (51474069); China Postdoctoral Science Foundation funded project (2016M591510); Natural Science Foundation of Heilongjiang Province (E2016007); City University of Hong Kong Applied Research (9667122); City University of Hong Kong Strategic Research (7004644).